Available online at www.sciencedirect.com

SCIENCE DIRECT®

Earth and Planetary Science Letters 222 (2004) 1037–1050

EPSL

www.elsevier.com/locate/epsl

Stress balance above subduction: application to the Andes

L. Husson*, Y. Ricard

Ecole Normale Supérieure de Lyon, Laboratoire des Sciences de la Terre, 46 allée d'Italie, 69364 Lyon Cedex 07, France

Received 19 November 2003; received in revised form 23 March 2004; accepted 26 March 2004

Abstract

The frequent changes in tectonic and morphological evolutions of active plate margins suggest that similar processes drive apparently antagonistic tectonics. We address the problem by a thin viscous sheet approach where the governing stresses are restricted to interplate traction, buoyancy and viscous stresses. Various cases are explored, from compression to extension, leading to dismiss corner-flow-driven models and to favor interplate traction-driven models. From the topography of the Andes, we determine the magnitude and profiles of the current stresses beneath the Andes at various locations. The total transmitted force is about 9×10^{12} N m^{-1}. Shear stresses at the boundaries of the deforming lithosphere range between 25 and 110 MPa and almost balance the buoyancy stresses due to crustal thickening, the remaining difference being the viscous stresses. The deviatoric stress is less than 10 MPa and the effective viscosity of the Andean lithosphere is as low as $\sim 3 \times 10^{21}$ Pa s. Maximum compression is located in the Eastern side of the Andes, matching the geological observations, but we find that the current stress regime is insufficient to explain the present-day elevation. This suggests that interplate traction was slightly stronger in the past when the Neogene plate convergence was faster, and this decrease in interplate traction implies that high and steep parts of the Andes cannot be sustained anymore. The shape of the Altiplano can be explained by a weak lateral variation of the viscosity, which allows the high plateau to be constructed in the characteristic time span of Andean building.

Keywords: subduction; stress; topography; crustal deformation; fluid dynamics

1. Introduction

Although the main characteristics of subductions are similar anywhere, their morphological and tectonic expressions vary from intensely compressive to extensive through intermediate settings, so that the intraplate stress field has been intensively discussed and remains the focus of many studies (e.g. [1]). Within cratons, the intraplate stress field is mainly neutral or compressive, but it is fairly common to see combined extensional and compressional settings in convergent systems. The Aegean sea and the Tonga trench display extensional patterns, the Japan sea and Italy show coeval extensional and compressional features, while the Andes undergo compression with some areas of neutral/extensional regimes. The tectonic regime also varies through time: for instance the Basin and Range evolved from the Laramide compression to the present-day extension [2]. These changes of tectonic regimes suggest that the physical processes governing deformation differ only slightly from one geodynamic setting to another.

* Corresponding author. Present address: Collège de France, Chaire de Géodynamique, Europôle de l'Arbois 13545, Aix-en-Provence, France.

E-mail address: husson@cdf.u-3mrs.fr (L. Husson).

0012-821X/$ - see front matter © 2004 Elsevier B.V. All rights reserved.
doi:10.1016/j.epsl.2004.03.041

Topography is the consequence of stresses applied to tectonic plates and of their evolution through time. All stresses in Earth are the consequences of lateral variations in the internal density. Plate-driving stresses are mostly resisted by basal shear on the asthenosphere. The role of crustal or lithospheric density variations has been emphasized by many authors [3–11]. Using the thin viscous sheet approximation, Wdowinski et al. [12] concluded that the Andean topography is the consequence of a basal shear induced by corner-flow circulation while the internal sources of stresses due to crustal thickening were neglected. We propose herein an alternative mechanism for mountain building where forces acting on the plate boundaries are balanced by internal stresses arising from crustal thickness variations. We first address the problem using theoretical cases to decipher which forces can be responsible for various geodynamic settings. We then use the observed topography to quantify the stresses acting on the Andean margin, and evaluate the results by considering a time-dependent model.

2. The model

2.1. Thin viscous sheet approximation

The derivation of the thin viscous sheet model for the lithosphere has been discussed in detail in various papers dealing with continental deformation (e.g. [4,13]) and we only briefly discuss the assumptions. The thin sheet model is based on the vertical integration of the Navier–Stokes equations coupled with mass conservation. The lithosphere is stiff enough with respect to the underlying mantle that the vertical variations of the horizontal velocity can be neglected. The lithosphere is also thin enough with respect to the scale of the deformations under consideration that the horizontal gradients of the stresses are negligible with respect to the vertical gradients [14].

In the lithosphere we define σ_{ij}, τ_{ij} and P to be the total stress tensor, the deviatoric stress tensor and the pressure, respectively (i or j stand for x or y as we only derive a two-dimensional model),

$$\sigma_{ij} = \tau_{ij} - P\delta_{ij}. \tag{1}$$

We assume that the lithosphere behaves like an incompressible viscous fluid with

$$\tau_{ij} = \eta\left(\frac{\partial u_i}{\partial x_j} + \frac{\partial u_j}{\partial x_i}\right), \tag{2}$$

where the average effective viscosity of the lithosphere η can be constant, laterally variable or even some non-linear function of the stress tensor. u_i either represents the horizontal velocity or the vertical velocity.

Assuming that the bottom of the lithosphere is subjected to a shear stress Σ (we choose $\Sigma = -\sigma_{xz}$ ($z=0$) so that $\Sigma>0$ on the left margin of the plate induces compression) while the upper surface is stress free. Within the thin sheet approximation, integrating the vertical force balance equation, the vertical equilibrium becomes

$$\frac{1}{2}\frac{(z-L-h)^2}{L+h}\frac{\partial \Sigma}{\partial x} + \sigma_{zz}(z) = \int_{L+h}^{z} \rho g \, \mathrm{d}z, \tag{3}$$

where ρ is the density, g the gravitational acceleration and z the depth measured from the bottom of lithosphere of thickness L. The upper surface topography is at the position $L+h$ ($z \le L+h$). In the following, we set L to 100 km, assuming that the lithospheric mantle diffuses thermally faster than its vertical growth (Fig. 1).

In the usual thin plate approximation, basal tractions are assumed not to be significant. When accounted for, the first term on the left of Eq. (3) is often neglected as the horizontal stress variations are assumed to be with much longer wavelengths than the lithospheric thickness, but this approximation would not be very good for steep mountain belts such as the Andes, where there must be significant tractions.

We integrate vertically the equation expressing the horizontal equilibrium over the lithosphere thickness. One gets

$$\frac{\partial}{\partial x}\int_0^{L+h} \sigma_{xx}\mathrm{d}z + \Sigma = 0. \tag{4}$$

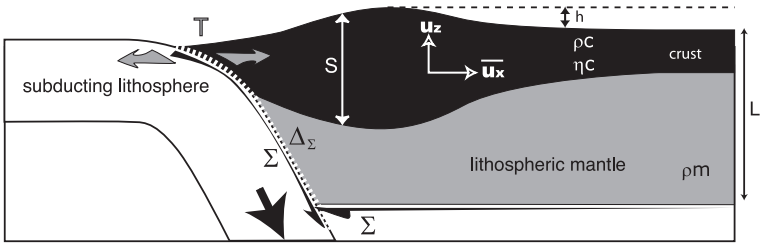

Fig. 1. Sketch model of the subduction zone. See text for legends.

The horizontal total stress σ_{xx} can now be replaced by the sum of the deviatoric and vertical total stresses; $\sigma_{xx}=\tau_{xx}-\tau_{zz}+\sigma_{zz}$. Using Eqs. (2) and (3), we obtain

$$4L\frac{\partial}{\partial x}\bar{\eta}\frac{\partial \bar{u}}{\partial x}+\Sigma=-\frac{\partial}{\partial x}\int_0^{L+h}\mathrm{d}z\int_{L+h}^{z}\rho g\,\mathrm{d}z'-\frac{1}{6}\frac{\partial^2\Sigma}{\partial x^2}L^2 \quad (5)$$

which describes the horizontal equilibrium (leaving out in the Σ derivatives the terms of lower importance, in h^2 and hL), averaged over the thickness of the lithosphere. Wdowinski et al. [12] implicitly neglected the second order term $(L^2/6)$ $(\partial^2\Sigma/\partial x^2)$. The influence of the density variations only arises from crustal thickness variations and density variations between the lithospheric mantle and asthenosphere are neglected. We can therefore define an isostatic crustal thickness $S=h\rho_m/(\rho_m-\rho_c)$, where ρ_m and ρ_c are the mantle and crust densities, respectively. h is defined with respect to a crust of null thickness (i.e. $h=0$ when $S=0$, and a continent with a typical crustal thickness $S_0=35$ km corresponds to a topography of 4375 m). For simplicity, we omit the averaging symbol (overline) for vertically averaged quantities ($\bar{u}$ and $\bar{\eta}$ in Eq. (5)) in the following. After some algebra Eq. (5) gives the following horizontal stress balance equation

$$4L\frac{\partial}{\partial x}\eta\frac{\partial u}{\partial x}=\frac{\rho_c g}{2}\left(1-\frac{\rho c}{\rho m}\right)\frac{\partial S^2}{\partial x}-\Sigma-\frac{1}{6}\frac{\partial^2\Sigma}{\partial x^2}L^2. \quad (6)$$

It couples the basal shear Σ, the deviatoric stress $T=-4\eta\partial u/\partial x$ ($T>0$ corresponds to compression), and the buoyancy forces related to S^2. The fact that S^2 (or Sh) rather than S controls the deformation is sometimes called the density moment rule [15].

A non-dimensionalization of Eq. (6) can be performed (e.g. using the length scale L and reference velocity and viscosity, u_0 and η_0) which leads to the introduction of the Argand number Ar [16], which writes accordingly to [4]

$$Ar=\frac{\rho_c g L^2}{2\eta_0 u_0}\left(1-\frac{\rho_c}{\rho_m}\right). \quad (7)$$

Ar indicates the capability of the lithosphere undergoing buoyancy forces to deform. However, non-dimensional quantities do not simplify the following discussions and we keep dimensional values.

Additionally, for incompressible fluids, the time-dependence of the crustal thickness S is given by:

$$\frac{\partial S}{\partial t}+S\frac{\partial u}{\partial x}+u\frac{\partial S}{\partial x}=0. \quad (8)$$

By multiplying Eq. (8) by $2S$, one obtains the transport equation of the density moment [17],

$$\frac{\partial S^2}{\partial t}+2S^2\frac{\partial u}{\partial x}+u\frac{\partial S^2}{\partial x}=0. \quad (9)$$

Eqs. (6) and (9) are the governing equations of the model (see also [18]).

2.2. General comments

The transport Eq. (9) assumes local mass conservation. This assumption may be flawed in situations with erosion, sedimentation or magmatic addition. Mass variations could be taken into account by a source term in Eq. (8) to account for the net material addition or removal and by a diffusive term to represent transport with erosion and sedimentation.

We do not discuss these processes which affect the velocities (Eq. (9)) but not the stress balance (Eq. (6)).

We only account for lateral variations of density due to changes in crustal thickness. In fact, a dense lithospheric mantle would favor gravitational instabilities. Considering a lithospheric mantle with thickness $L-S$ has a density ρ_L slightly larger than the asthenospheric mantle density ρ_M, the Argand number Ar (Eq. (7)) should be written

$$Ar = \frac{gL^2}{2\eta_0 u_0}\left[\rho_c\left(1-\frac{\rho_c}{\rho_m}\right)+\rho L\left(1-\frac{\rho L}{\rho_m}\right)\frac{(L-S)^2}{S^2} + 2\rho_c\left(1-\frac{\rho L}{\rho_m}\right)\frac{(L-S)}{S}\right]. \quad (10)$$

Ar now includes the lithospheric mantle and is positive as long as $L \le 4S$ (assuming $\rho_c = 2800$ kg m^{-3}, $\rho_m = 3200$ kg m^{-3} and $\rho_L = 3225$ kg m^{-3}). If $L < 4S$, the dynamics remains qualitatively similar to that described herein although the stabilizing role of internal loads becomes less important. If $L > 4S$, the lithosphere becomes unstable by Rayleigh–Taylor instability. The long-term stability of continents suggests that Ar generally remains positive.

The existence of strong crustal variations between two tectonic units of different crustal thicknesses has to be associated with a change in deviatoric stresses. The x-integration of Eq. (6) across a discontinuity $\Delta S^2 = S^2(0^+) - S^2(0^-)$ of the crustal density moment (strictly speaking, the approximations imply that the crustal density moment change must occur over distances larger than the lithosphere thickness), implies a jump in the deviatoric stress $\Delta T = T^- - T^+$,

$$T^- - T^+ = \frac{\rho_c g}{2L}\left(1-\frac{\rho_c}{\rho_m}\right)(S^2(0^+) - S^2(0^-)), \quad (11)$$

(provided that the two units have similar lithospheric thicknesses L). Indeed, at a passive margin, the assymetry in crustal thickness is equivalent to an extensive stress applied at the continent boundary (~ 20 MPa for $L = 100$ km and a continental crust thickness $S = 35$ km). This extensive stress along the passive margins of South East Asia favors the southeastward extrusion along the collision of India with Asia. The tendency of thick continents to be under extension may be partially counteracted by their dense lithospheric roots that reduces the effective Ar.

By the horizontal integration of Eq. (6) between two tectonic units a and b of same crustal thickness, one gets

$$-L(T^a - T^b) = \int_a^b \Sigma + \frac{1}{6}\frac{\partial^2 \Sigma}{\partial x^2} L^2 \mathrm{d}x. \quad (12)$$

It shows that the change of stress between two tectonic units of same crustal thickness only depends on the basal friction. For instance, the stress change between the two sides of a mountain belt does not depend on the topography of the belt itself.

The system of Eqs. (6) and (9) can have motionless solutions (a zero vertically averaged horizontal velocity u) when the basal shear stress imposed beneath the lithosphere are exactly resisted by the stresses due to variations in the crustal structure.

$$\Sigma + \frac{1}{6}\frac{\partial^2 \Sigma}{\partial x^2} L^2 = \frac{\rho_c g}{2}\left(1-\frac{\rho_c}{\rho_m}\right)\frac{\partial S^2}{\partial x}. \quad (13)$$

In this case of steady state, the stresses at the base of the lithosphere can be deduced from the surface topography.

The lithosphere of the Earth is not in steady state and we will in the following discuss several time-dependent scenarii involving different distributions of stresses. They include compression/tension T at the plate boundary, and traction Σ at its base, either driving or resisting. At this stage, no attempt is made to reproduce a given geological setting.

2.3. Theoretical cases: mountain building at plate margin

We now consider situations where the crust has a uniform thickness S_0 at time $t = 0$ and where the viscosity is uniform and constant. A few experiments introducing a non-linear rheology in our model gave results that differ from the standard runs less than the obvious uncertainty due to the inhomogeneous structure of the lithosphere. To maintain the crust at a steady state, an initial deviatoric stress T_0 has to be applied $T_0 = \rho_c g/(2L)\ (1-\rho_c/\rho_m)\ S_0^2$ at $x = 0^-$. The simplest way to deform the lithosphere is to apply at the plate margin ($x = 0^-$) a deviatoric stress $T_0 + \delta T$

without any shear beneath the lithosphere, $\Sigma(x>0)=0$. According to (11) the deviatoric stress at $x=0^+$ is

$$T^+ = \delta T + \frac{\rho_c g}{2L}\left(1-\frac{\rho_c}{\rho_m}\right)(S_0^2 - S^2(t,x^+)). \qquad (14)$$

The two deviatoric stresses T^+ and δT are identical at $t=0$ but then, T^+ decreases with $S^2(t,x^+)$. The horizontal plate velocity is set to 0 at a distance D away from the free border of the plate. Without bottom shear ($\Sigma=0$), Eq. (6) implies that the deviatoric stress is uniform and according to Eq. (8), the crustal thickness varies in the first time steps as

$$\frac{dS}{S} = \frac{T^+}{4\eta L}dt. \qquad (15)$$

A normal stress at a plate boundary (e.g. in a collision situation) does not deform the plate locally but uniformly. The situation of uniform deformation is unlike most everyday situations where the dynamics is dominated by inertia and where the application of a normal stress tends to produce local deformation (a car hit in the front deforms in the front). Note that because T^+ decreases when S increases, the final height is reached when $T^+=0$.

A situation where the basal traction Σ decreases from the edge toward the hinterland roughly mimics interplate traction at subduction zones. In the first time steps, the deviatoric stress increases with the distance to the trench (again, thickening occurs away from the trench),

$$\frac{dS}{S} = \frac{\Sigma}{4\eta L}dt. \qquad (16)$$

A similar situation is obtained in Fig. 2 where the shear below the lithosphere exonentially decreases as $\Sigma=\Sigma_0\ \exp(-x/\Delta_\Sigma)$. The crust has an initial uniform thickness S_0. A topography is generated (Fig. 2) over the basal shear zone, with a -quasi-exponentially decreasing slope according to Eq. (16). Away from the zone undergoing interplate traction, a high plateau develops with a final elevation $H\sim\int_0^x(\Sigma+\frac{L^2}{6}\frac{\partial^2\Sigma}{\partial x^2})dx/\rho_c g S_0$. The deviatoric stress (Fig. 2) evolves from compressive to neutral when the steady state (Eq. (13)) is reached.

To explain a topography near the plate margin, a basal shear stress toward the trench can be invoked. A

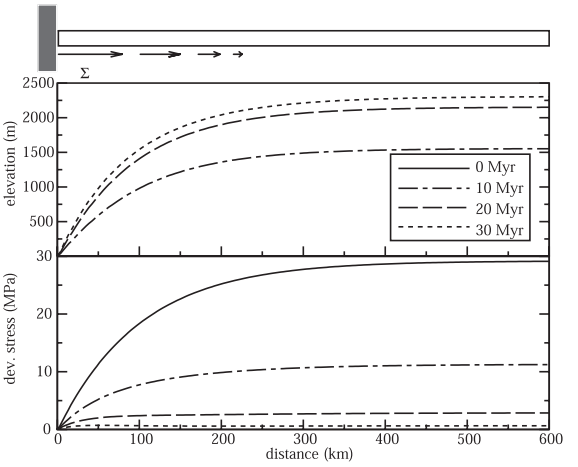

Fig. 2. Elevation and deviatoric stress induced by a basal traction $\Sigma=\Sigma_0 e^{-x/\Delta\Sigma}$ (toward the hinterland), with $\Sigma_0=25$ MPa, $\Delta_\Sigma=100$ km, $L=100$ km, $\eta=5\times10^{21}$ Pa s, $\rho_c=2800$ kg m^{-3} and $\rho_m=3200$ kg m^{-3}. The initial crustal thickness is $S_0=35$ km and the plate length $D=7000$ km.

corner-flow has indeed been mentioned for mountain building at plate margins (e.g. [12]). This situation corresponds to that depicted in Fig. 3 where we used the same parameters as in Fig. 2, with an exponentially increasing traction toward the trench, although traction for the corner-flow model is often described as proportional to $1/x$. A zero velocity at the trench is required. It implies that a deviatoric stress can build up at the plate margin, resisting the rising stresses induced by the growing topography. As previously, the deviatoric stress decreases during the orogeny (Fig. 3).

In real Earth, the plate motion is resisted by a drag at the lithosphere/asthenosphere boundary. To simulate a subduction zone, we add a resistive stress proportional to the lithospheric velocity u to the previously considered driving basal shear stress, so that Σ is now replaced by $\Sigma-ku$. The shear stress $-ku$ could mimic the traction at the base of the lithosphere of the Couette flow induced by the lithospheric motion [18]. Eq. (6) becomes accordingly

$$4L\frac{\partial}{\partial x}\eta\frac{\partial u}{\partial x} = \frac{\rho_c g}{2}\left(1-\frac{\rho_c}{\rho_m}\right)\frac{\partial S^2}{\partial x} - \Sigma + ku - \frac{L^2}{6}\frac{\partial^2(\Sigma-ku)}{\partial x^2}, \qquad (17)$$

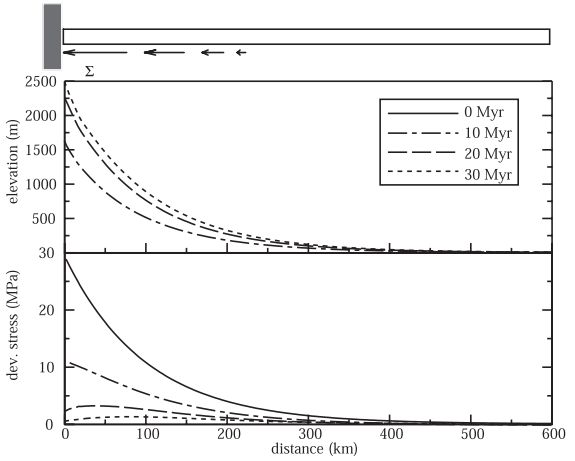

Fig. 3. Deviatoric stress and elevation induced by a basal traction $\Sigma = -\Sigma_0 \exp(-x/\Delta_\Sigma)$ (toward the trench) below the overriding plate. This traction roughly mimics the effect of a corner-flow circulation. Parameters are those of Fig. 2.

When Σ is directed toward the trench ($\Sigma<0$, corner-flow, Fig. 4), the simulations are fairly similar to those of Fig. 3. However, the motion of the plate is now resisted by a passive drag of the mantle, and a depression associated with extension is expected hinterland. If the shear stress is directed toward the trench ($\Sigma>0$, interplate traction, Fig. 5), the deviatoric stress

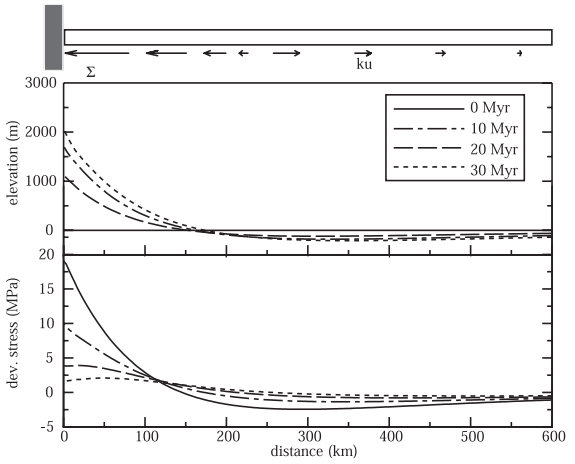

Fig. 4. Elevation and deviatoric stress induced by a corner-flow driving traction below the overriding plate (as in Fig. 3), resisted by a passive drag *ku* at the base of the lithosphere. The resistance k is 3.9×10^{16} Pa s m^{-1} (i.e. 10 MPa at 0.8 cm/year). Other parameters are those of Fig. 2.

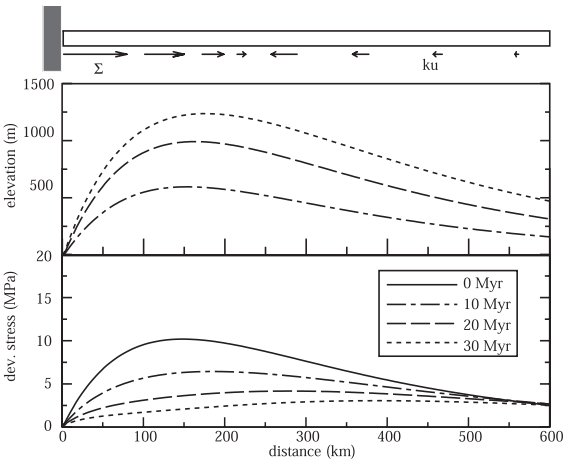

Fig. 5. Elevation and deviatoric stress induced by an exponentially decreasing interplate traction below the overriding plate (as in Fig. 2), resisted by a passive drag at the base of the lithosphere. Parameters are those of Fig. 4.

first increases and then drops when the passive drag gets higher than the transmitted stress. A relief builds up at the plate margin and only compression is expected. A neutral stress is achieved when the steady state is reached.

When the basal traction is directed away from the trench, the maximum velocity is produced next to the trench and decreases toward the hinterland (Fig. 6, top). The corner-flow model predicts velocities directed toward the trench, of lower magnitudes (Fig. 6, bottom). A velocity peak is reached where the resistance gets stronger than the corner-flow shear and extension is then induced hinterland.

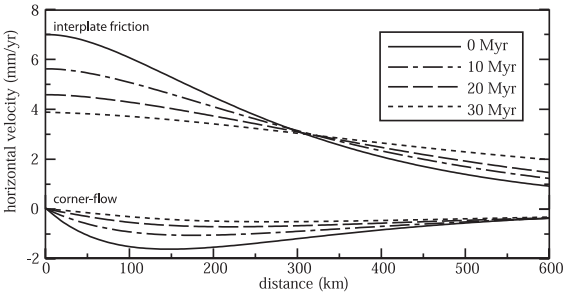

Fig. 6. Horizontal velocities when tectonics is driven by interplate traction (top) and when tectonics is driven by corner-flow (bottom). Positive velocities are directed toward the right hand side. The situations are those depicted in Figs. 4 and 5.

These theoretical cases highlight the sensitivity of the predicted topography on different models. One is the corner-flow model [12], and the other suggests that interplate traction is responsible for mountain building. The main difference between these models is the sense of the basal shear traction (toward the trench in the first model, toward the hinterland in the second). The corner flow model pulls the upper plate toward the trench while interplate traction pushes the overriding plate toward its hinterland. In [12], there is no interaction between the lithosphere and the mantle far from the subduction corner (i.e. they implicitly assume $k=0$) and no extension is then induced hinterland. In our simulation, on the contrary, a passive drag implies a bulk extension of the overriding plate hinterland comparable in magnitude to the bulk shortening across the orogen. Geodetic measurements over the Andes [19–21] and the Himalayas [22,23] as well as the global intraplate stress map [1] indicate a compression rather than extensional stress regime behind mountain belts associated with subduction zones, supporting the notion that interplate tractions play a more important role than counterflow in deformational dynamics in these areas.

2.4. Theoretical cases: from gravitational collapse to back-arc opening

Subduction zones can also be associated with extension rather than with compression when the stresses at or near the plate margin either decrease and cannot support furthermore a preexisting topography, or become intrinsically extensive. This change of boundary conditions may be related to the slowing down of the normal subduction rate (South Tibet [24] and South Peru [25]), to the stopping of subduction (Basin and Range [2]) or to back-arc opening (Aegean sea [26]).

Gravitational collapse can be illustrated by decreasing the compressive stresses. In Fig. 7, we compute the evolution of the topography of Fig. 5 when the interplate traction is suddenly reduced to zero at time $t=30$ Ma. The initial situation depicted by a solid line in Fig. 7 corresponds to the last situation (dashed line) of Fig. 5. During the transition toward a new equilibrium state, the tectonic

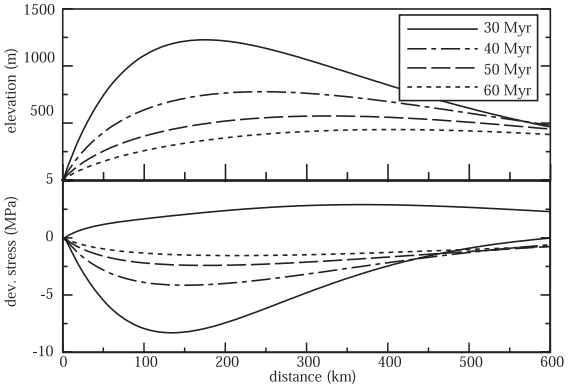

Fig. 7. Elevation and deviatoric stress for a collapsing pre-existing topography. The situation at 30 Ma in Fig. 5 is suddenly submitted to zero interplate traction ($\Sigma=0$). Solid lines show the situation just before and after the shear stress is set to zero. Other parameters remain as in Fig. 5.

stresses become extensive and the mountain range collapses. The maximum extension is located where the mountain reaches its highest elevation. The existence of a deviatoric stress at the plate margin able to sustain a 35-km-thick crust precludes any further thinning. A more quantitative illustration of this process focussed on South Peru will be presented in the following.

A further evolution toward an oceanic domain can occur when the deviatoric stress at the plate margin can no longer sustain the thickness of the continental crust. In the previous models, only basal traction was assumed. In order to account for slab retreat, an extensional deviatoric stress, T^+, can be imposed at the trench level (Fig. 8). During the first stage, the deviatoric stress is extensive next to the trench ($T^+<0$) but can remain compressive hinterland as in this simulation if $LT^+ + \int_0^x (\Sigma + L^2/6\partial^2\Sigma/\partial x^2)\mathrm{d}x > 0$. As the topography gently increases, stresses gradually become neutral hinterland as a marginal basin widens. Such scenario may explain the mild extensive situations at plate margins (e.g. in the Longitudinal Valley of Chile).

Nevertheless, we neglected significant specificities that are beyond the scope of this paper, such as local mass conservation which does not hold anymore due to magma production in back arcs situations. In an end member situation, the total amount of extension correspond to magma production rather than to crustal

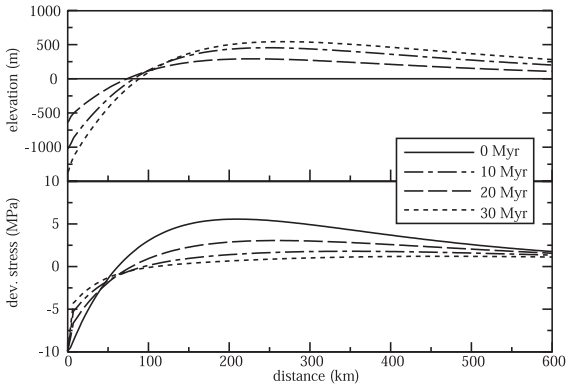

Fig. 8. Elevation and deviatoric stress induced by an exponentially decreasing interplate traction below the overriding plate, resisted by the drag at the base of the lithosphere as in Fig. 5. In addition, a − 10 MPa normal deviatoric stress is imposed as a right boundary condition. Such forcing mimics the effects of trench suction. Parameters are those of Fig. 5.

thinning. Still, it would affect the velocities but not the stress balance.

3. Application to the Andes

3.1. Fitting the topography

The Andean belt is located over the eastward subduction of the Nazca plate below South America. It is characterized by a thick crust up to 70 km below the Eastern Cordillera of Bolivia that compensates the topography (e.g. [27,28]).

Let the interplate traction and the deformation velocity have sigmoidal variations with x, as

$$\Sigma = \frac{\Sigma_0}{2}\left(1 - \tanh\frac{(x - x_\Sigma)}{\Delta_\Sigma}\right), \tag{18}$$

$$u = \frac{u_0}{2}\left(1 - \tanh\frac{(x - x_u)}{\Delta_u}\right). \tag{19}$$

These profiles allow Σ and u to decrease from Σ_0 and u_0 at the trench to zero hinterland over the lengths Δ_Σ and Δ_u. The distance at which the traction and velocities are halved are x_Σ and x_u. Any monotonic function decreasing from a maximum near the trench to zero hinterland could have been used but a sigmoidal variation for the velocity field is in agreement with the velocity profiles inferred from direct measurements (e.g. [29]).

Assuming isostasy, we compute from the observed topography S the term of Eq. (17) related to the density moment $1/2\rho_c g(1 - \rho_c/\rho_m)\partial S^2/\partial x$ and deduce the quantities Σ_0, x_Σ, Δ_Σ, u_0, x_u, Δ_u, η and k by a generalized least square adjustment of Eq. (17) for various Andean profiles (Table 1).

The viscosity η is considered as uniform. We choose four topographic profiles perpendicular to the trench (averaged over 200 km large bands, see Fig. 9). The case of South Peru where extensive tectonics is observed will be discussed separately. The topographies are depicted in Fig. 10 (left column). The associated $1/2\rho_c g(1 - \rho_c/\rho_m)\partial S^2/\partial x$ functions related to crustal variations are shown in the right column (thick lines). In each case, these functions are initially positive (along the western flank of the Andes) then abruptly change sign, become moderately negative and eventually reach zero. The interplate traction term (dashed lines), deduced from the inversion, closely fits the western segment of positive $\partial S^2/\partial x$. The resistive term (dotted lines) balances the negative part of $\partial S^2/\partial x$. The remaining term proportional to $\partial^2 u/\partial x^2$ (long dashed) is always very small. It represents the variations of the deviatoric stresses. The stress balance of the orogen naturally evolves toward a cancellation of this term.

3.2. Quantifying the stresses

Interplate traction varies along-strike as both its amplitude and the width of the traction zone are directly related to the distance to the trench of the maximum elevation (Fig. 10). Interplate traction

Table 1
Deduced parameters from the inversion of the Andean topography, Eqs. (17), (18) and (19)

	Peru	Altiplano	N. Chile	S. Chile
Σ_0 (MPa)	108	26	70	27
x_Σ (km)	26	175	55	20
Δ_Σ (km)	50	80	100	47
u_0 (mm/year)	5	7	3.5	2
x_u (km)	280	650	280	380
Δ_u (km)	120	100	80	200
η (Pa s)	2.15×10^{21}	1.66×10^{21}	4.28×10^{21}	4.8×10^{21}
k (Pa s m^{-1})	2.2×10^{17}	5.4×10^{16}	3.2×10^{17}	1.0×10^{17}

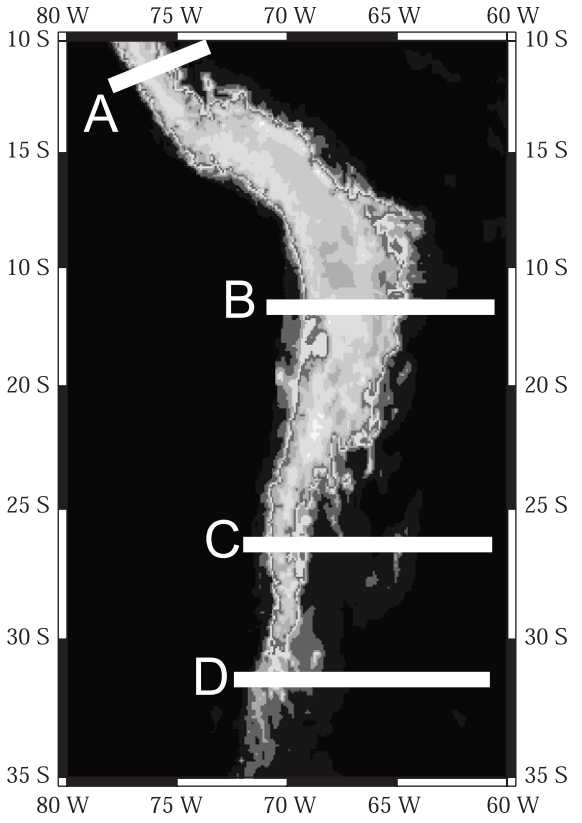

Fig. 9. Topography of the Andes. Location of the four reference profiles (across Central Peru (A), North (B), Central (C), and South (D) Chile).

ranges between 25 and 110 MPa, consistent with [30,31]. The shorter wavelength of the Peruvian Andes requires a stronger traction over a shorter distance Δ_Σ than below the Altiplano section. The total transmitted force from the subducting plate, $\int_0^\infty (\Sigma + \frac{L^2}{6}\frac{\partial^2 \Sigma}{\partial x^2})$ dx is similar for the three mature profiles A, B and C ($\sim 9 \times 10^{12}$ N m^{-1}), and only for D this force is lower ($\sim 2.3 \times 10^{12}$ N m^{-1}).

The Andean subduction is commonly divided along-strike into several panels which correspond to the subduction angle of the Nazca plate. North and South of the Altiplano high plateau (18°S to 28°S), the slab segments subduct with a shallow angle (A and C). At the level of the Altiplano (B) and also beneath South Chile (D), the slab subducts with a steep angle. The traction profiles are not correlated to the present-day inclination of the Benioff–Wadatti zone at greater depth. Because slab bending changed through time in the Andes [32], the present-day stress balance reflects an average of the whole history of interplate traction.

The deviatoric stresses associated with the present-day tectonic deformation are given by $4\eta\partial u/\partial x$. For the four profiles, the deviatoric stresses are less than 10 MPa (see Fig. 11). The maximum compression and the width of the compressive zone are free parameters for the inversion. Maximum compression occurs in the Sub-Andean Zone, in agreement with geological observations (e.g. [33]).

From the previous inversion we have obtained the shape of the horizontal velocity and the amplitude of the deviatoric stresses (Fig. 11). Geodetic GPS measurements in the Andes confirm a maximum shortening in the foreland. They indicate a maximum East–West shortening across the belt of about 4 cm/year but the secular deformation is less than 1 cm/year [29,21]. A similar value can be estimated from geological records. Total Neogene shortening is assumed to range between 190 and 250 km in the Central Andes [33,34], which corresponds to 7 to 9 mm/year average deformation for 27 Ma, and probably 10 mm/year for the last 10 Ma [29].

Combining this velocity information with the deviatoric stresses, we estimate a viscosity in the range of 1.5 to 5×10^{21} Pa s, only a couple of orders of magnitude larger than the underlying mantle (4×10^{19} Pa s [35]). It represents an effective rheology averaged over the lithosphere, accounting for the softening of the lithosphere due to crustal faulting, fracturation and décollement levels. England [36], based on strain rates in extensional areas, mentioned that the lithosphere viscosity has to be about 10^{22} Pa s, and Wdowinski et al. [12] suggested that it can even be as low as 10^{21} Pa s in some places. We explain the low effective visosity of the Andean lithosphere by its pre-Andean history. The western margin of South America underwent several extensional events that thermally and mechanically weakened the lithosphere, particularly between 18°S and 28°S [37–39].

3.3. Time evolution

The previous inversions provide the current stress balance in the Andes, but may not reflect the past stress balance responsible for the overall growth of the

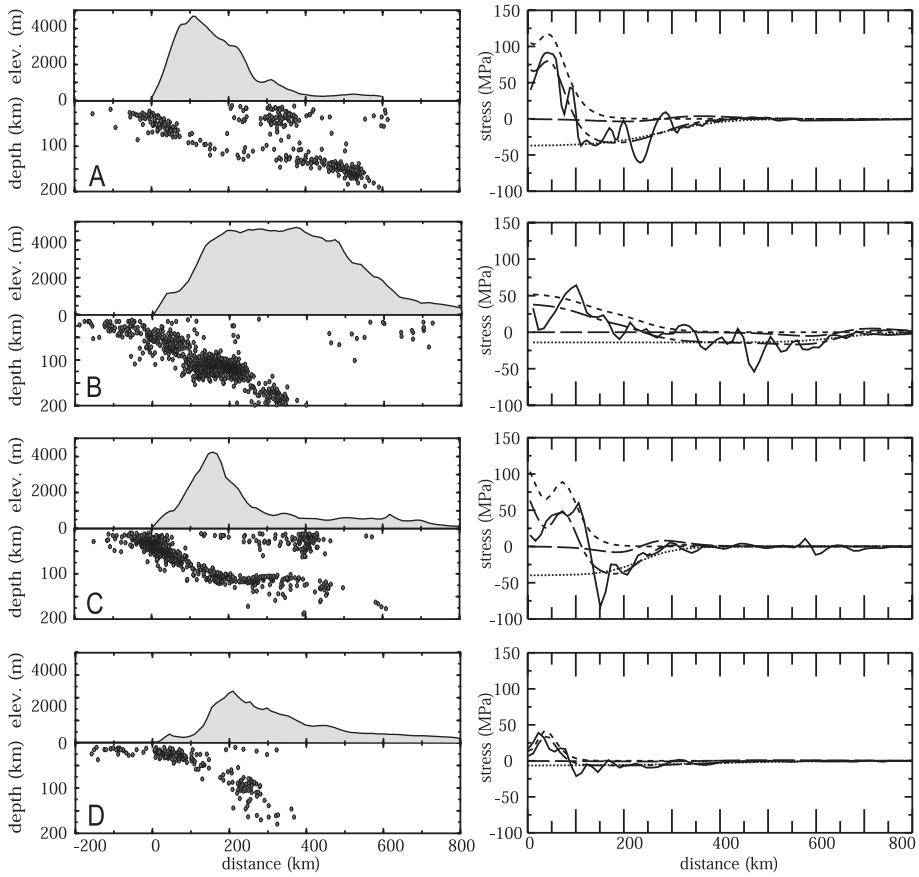

Fig. 10. Left column: topographic profiles A, B, C and D corresponding to Fig. 9. Earthquake epicenters underlining Benioff zone of the Nazca plate are also plotted. Right column: $1/2\rho_c g(1-\rho_c/\rho_m)\partial S^2/\partial x$ profiles (solid lines). These profiles can be balanced by the sum of an interplate traction (dashed lines), a resistive basal shear (dotted lines) and an internal deviatoric stress term (long dashed) computed from a generalized least-squares fit of Eq. (6). The sum of the three last terms (dotted-dashed) give good fits to the observations (solid lines).

Andes. Indeed, interplate traction profiles may have changed during the orogeny. We now test whether or not the present-day boundary conditions are appropriate to reconstruct the present-day situation, starting with an homogeneous plate and integrating Eqs. (6) and (9) through time. For each section, we take the parameters Σ, x_Σ, Δ_Σ, k and η deduced from the previous fits (Table 1). Contrarily to the previous sections, the velocity profiles are not constrained to have a priori sigmoidal shapes but are deduced from time integration.

3.3.1. General models for the Andes

Choosing the present-day traction profiles as constant boundary conditions through time allows the Andean belt to be reconstructed; however, in order to reproduce the current topography in the time range of the Andean orogeny (i.e. $\sim$ 27 Ma), the present-day interplate traction profiles are too low and have to be increased by 7 to 30 MPa (Fig. 12). Profile B, across the Altiplano presents a tangible misfit as the high plateau shape cannot be reproduced. In S. Chile (C), the Longitudinal Valley on the western side is neglected.

The convergence rate between the Nazca and South American plates strongly increased since 27 Ma and gradually decreased until present [40,41]. One can assume that interplate traction during the Andean orogeny decreased accordingly to the convergence rate. The fact that our time-dependent simulations

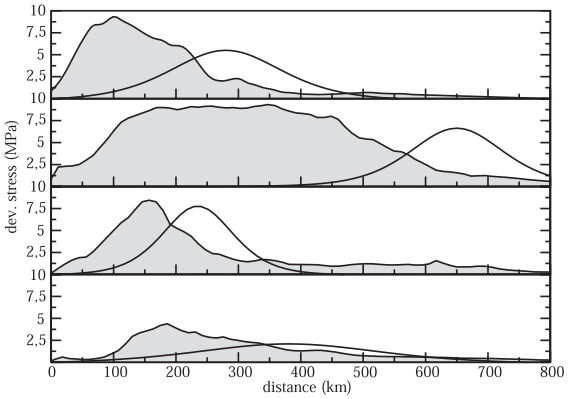

Fig. 11. Predicted deviatoric stresses for the four sections, according the stress balance shown in Fig. 10. In all cases the largest compressive stresses at present-day occur in the eastern fold and thrust belt. The topography is shown in shadings.

requires larger interplate tractions than at present-day reflects such an evolution.

3.3.2. High plateaus: the Altiplano example

A better fit to the observed topography of the Altiplano than in Fig. 12 could be obtained by weakening the rheology of the Andean lithosphere in order to confine and enhance the deformation of the Eastern Cordillera. A thermally thinned lithosphere has indeed been invoked to explain the building of the Altiplano [42–44]. Moreover, an Early Neogene lithospheric stretching has been active at the level of the Altiplano [37]. Fig. 13 shows the predicted topography after 27 Ma, using a moderate lateral viscosity increase under the eastern edge of the Cordillera (from 2.1×10^{21} to 6.3×10^{21} Pa s). The variation of the effective viscosity is also a way to account for the strong décollement, in the brittle deformation domain, where the Brazilian craton subducts.

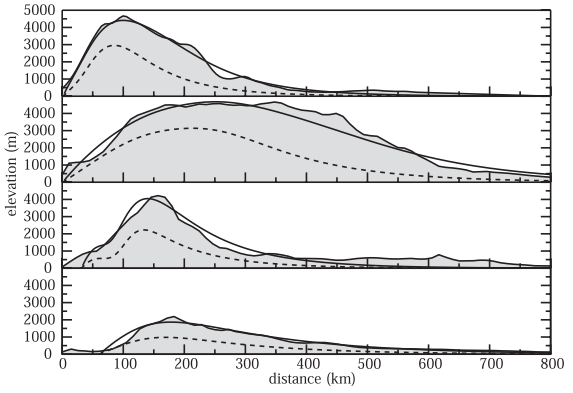

Fig. 12. Forward modeling of the four sections. In each case, the lines show the topographic profile at 10 (dashed) and 27 Ma (solid). Boundary conditions and viscosities (from 1.5×10^{21} to 5×10^{21} Pa s) are deduced from the inversion of the topography (Fig. 10) except interplate tractions that have been raised by 7 to 30 MPa, accounting for the decrease in the convergence rate.

3.3.3. Extension in active mountain belts: the South Peruvian example

A neutral state of stress has been evidenced by the coeval normal and inverse tectonic regimes in mountain belts such as the Alps (e.g. [45]), the Andes [46,47,25], or Tibet [24]. In the Andes, it has been described between 13°S and 18°S. This segment is the most oblique to the present-day convergence direction. Although still controversial, paleomagnetic data (e.g. [48,49]) indicate that this segment probably rotated counterclockwise. Although the setting is obviously 3D this situation can be simulated assuming that the segment rotated 30° counterclockwise for the last 10 Ma and that only the traction component normal to the belt affects the 2D stress balance. The traction is then a function of the convergence angle between the two plates. After being Σ between 27 and 10 Ma, we reduce the interplate traction by cos θ where θ varies from 0 at 10 Ma to 30° at present. Fig. 14a depicts the evolution of interplate traction and of the associated maximum elevation through time. Boundary conditions are those given for the Peruvian segment (panel A, Figs. 9 and 10).

The deviatoric stress at present (after 27 Ma of orogeny) well matches the observations of extension in the high Andes and compression in the Sub-Andean

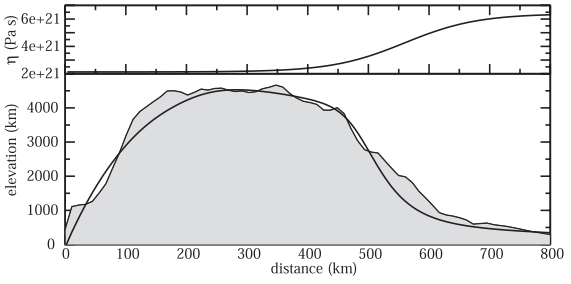

Fig. 13. Forward modeling of the Altiplano area at 27 Ma (bottom) introducing a lateral variation of viscosity (top). The interplate traction profile corresponds to that depicted in Fig. 10 panel B.

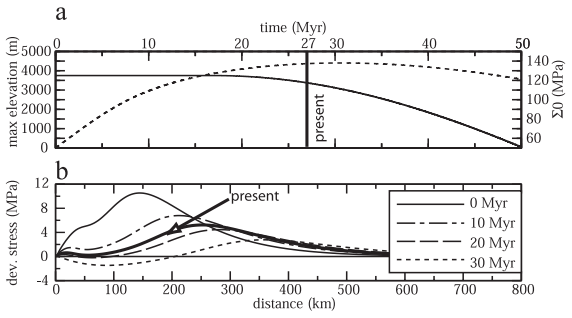

Fig. 14. Forward modeling for South Peru. Boundary conditions are the same as in Fig. 10 panel B. (a) Interplate traction (solid line) is assumed to decrease as the plate rotates at constant rate after 17 Ma (30° in 10 Ma). Until 25–30 Ma, the maximum elevation (dashed line) increases. (b) Deviatoric stress through time. The deviatoric stress becomes extensive where the elevation is maximum but remains compressive on the edges of the mountain belt. The present-day situation should correspond to 27 Ma, where the deviatoric stress cancels on the western side of the belt.

Zone (Fig. 14b). Of course, in our 2D model the extension can only be perpendicular to the belt while the observations indicate a significant along-strike component. If we assume arbitrarily that the rotation of the belt will continue in the future, the simulation predicts a general collapse of the topography. The tectonic stresses will be extensive everywhere but in the Brazilian craton where, according to Wdowinski et al. [12], the prevailing compressive stresses imposed by the subduction will still be acting.

The slowing down of the Nazca subduction should have the same impact and tends to shift the tectonic regime toward extension. It may be the case for the Quaternary extension in the North Peruvian segment.

So far we have neglected the Longitudinal Valley in the southern Andes, which becomes a significant feature in the southernmost section (D). This area features extensive focal mechanisms associated with the depression. The decrease in the convergence rate is likely associated to a decrease in the normal stress at the plate margin, leading to the onset of a situation comparable to that depicted Fig. 8.

4. Conclusions

Most tectonics settings and surface morphologies of plate margins can be understood and reconstructed using a thin sheet approximation. Interplate traction and resistive drag at the base of the lithosphere are the main controls of the tectonic regime at plate margins. The topography (more likely the crustal thickness variations) gives a first order feedback on the evolution of tectonics at plate margins.

Our model considers that topography is entirely supported by isostasy, and does not account for other forces like those arising from the elastic flexure of the downgoing lithosphere. The model also aims at reducing an intrinsically 3D problem to 2D: only across-strike deformation is considered and is averaged over the lithosphere thickness. A limitation comes from the assumption of local mass conservation that neglects erosion, delamination and magmatism. Corner-flow as a driving mechanism for Andean type tectonics can be discarded as it induces an extensive stress regime on the overriding plate.

The stress balance equation can be used to invert the topography and predict the present-day magnitudes and along-strike profiles of the stresses responsible for mountain building. In the Andes, we find that interplate traction range between 25 and 110 MPa. The total transmitted force is about 9×10^{12} N m^{-1} for the mature parts of the belt, consuming a significant amount of the plate tectonics driving forces. The topography of the Andes can be achieved in 25 to 30 Ma with a lithospheric viscosity between 1.5×10^{21} and 5×10^{21} Pa s, but only if the interplate traction is increased by 7 to 30 MPa with respect to the present-day stress balance. It outlines that the current topography reflects the history of the transmitted force as plate convergence was more vigorous in earlier periods of Andean orogeny.

Particular settings such as extension or high plateaus can often be reproduced by mild improvements of the model. In South Peru, the N–S extension can be explained by the increasing obliquity to the convergence of this segment of the Andes through time, which reduces the interplate traction. In fact, a slight change in the boundary conditions has an immediate impact as the tectonic equilibrium prevails (as outlined by the viscous stresses, which are almost one order of magnitude lower than the other stresses). This explains the frequent extensional tectonic regimes observed in various orogens. We also show in the case of the Altiplano that a very slight lateral viscosity variation is required for high plateaus to develop.

Acknowledgements

This work was supported by the Institut Français Pétrole. We wish to thank D. Coblentz and Ph. England for their reviews. This work also benefited from S. Medvedev's extreme meticulousness. ***[EB]***

References

[1] J. Reinecker, O. Heidbach, B. Mueller, 2003. The 2003 release of the World Stress Map (www.world-stress-map.org).
[2] T. Atwater, Implications of plate tectonics for the Cenozoic tectonic evolution of western North America, Bull. Geol. Soc. Am. 81 (1970) 3513–3536.
[3] E.V. Artyushkov, Stresses in the lithosphere caused by crustal thickness inhomogeneities, J. Geophys. Res. 78 (1973) 7675–7708.
[4] P. England, D. McKenzie, A thin viscous sheet model for continental deformation, Geophys. J. R. Astron. Soc. 70 (1982) 295–321.
[5] P. England, D. McKenzie, Correction to: a thin viscous sheet model for continental deformation, Geophys. J. R. Astron. Soc. 73 (1983) 523–532.
[6] L. Fleitout, C. Froidevaux, Tectonic stresses in the lithosphere, Tectonics 2 (1983) 315–324.
[7] G. Houseman, P. England, Crustal thickening versus lateral expulsion in the Indian–Asian continental collision, J. Geophys. Res. 98 (1993) 12233–12249.
[8] B. Wuming, C. Vigny, Y. Ricard, C. Froidevaux, On the origin of deviatoric stresses in the lithosphere, J. Geophys. Res. 97 (1992) 11729–11737.
[9] D. Coblentz, R.M. Richardson, M. Sandiford, On the gravitational potential energy of the Earth's lithosphere, Tectonics 13 (1994) 929–945.
[10] C.H. Jones, J.R. Unruh, L.J. Sonder, The role of gravitational potential energy in active deformation in the southwestern United States, Nature 381 (1996) 37–41.
[11] C.H. Jones, L.J. Sonder, J.R. Unruh, Lithospheric graviational potential energy and past orogenesis: implications for conditions of initial Basin and Range and Laramide deformation, Geology 26 (1998) 639–642.
[12] S. Wdowinski, R.J. O'Connell, P. England, A continuum model of continental deformation above subduction zones: application to the Andes and the Aegean, J. Geophys. Res. 94 (1989) 10331–10346.
[13] S. Medvedev, Yu. Podladchikov, New extended thin-sheet approximation for geodynamic applications: I. Model formulation, Geophys. J. Int. 136 (1999) 567–585.
[14] L. Fleitout, C. Froidevaux, Tectonics and topography for lithosphere containing density heterogeneities, Tectonics 1 (1982) 21–57.
[15] C. Froidevaux, B. Isacks, The mechanical state of the lithosphere in the Altiplano–Puna segment of the Andes, Earth Planet. Sci. Lett. 71 (1984) 305–314.
[16] E. Argand, La tectonique de l'Asie, Congrès Géologique International, Comptes-rendus de la XIII Session, 596 pp., Brussels, 1924.
[17] C. Lémery, Y. Ricard, J. Sommeria, A model for the emergence of thermal plumes in Rayleigh–Bénard convection and infinite Prandtl number, J. Fluid Mech. 414 (2000) 225–250.
[18] S. Ellis, P. Fullsack, C. Beaumont, Oblique convergence of the crust driven by basal forcing: implication for length-scales of deformation and strain partitioning in orogens, Geophys. J. Int. 120 (1995) 24–44.
[19] L. Leffler, S. Stein, A. Mao, T. Dixon, M.A. Ellis, L. Ocola, I.S. Sacks, Constraints on present-day shortening rate across the central eastern Andes from GPS data, Geophys. Res. Lett. 24 (1997) 1031–1034.
[20] M. Bevis, R. Smalley, T. Heering, J. Godoy, F. Galban, Crustal motion north and south of the Arica deflection: comparing recent geodetic results from the Central Andes, G^3, 1 (1999).
[21] G. Khazaradze, J. Klotz, Short- and long-term effects of GPS measured crustal deformation rates along the south central Andes, J. Geophys. Res. 108 (2003) 2289, doi: 10.1029/2002JB001879.
[22] R. Bilham, K. Larson, J. Freymueller, Idylhim members, GPS measurements of present-day convergence across the Nepal Himalaya, Nature 386 (1997) 61–63.
[23] K.M. Larson, R. Burgmann, R. Bilham, J. Freymueller, Kinematics of the Indo-Eurasian collision zone and GPS measurements, J. Geophys. Res. 104 (1999) 1077–1093.
[24] R. Armijo, P. Tapponnier, J.L. Mercier, H. Tonglin, Quaternary extension in southern Tibet: field observations and tectonic implications, J. Geophys. Res. 91 (1986) 13803–13872.
[25] J.L. Mercier, M. Sébrier, A. Lavenu, J. Cabrera, O. Bellier, J.F. Dumont, J. Machare, Changes in the tectonic regime above a subduction zone of Andean type: the Andes of Peru and Bolivia during the Pliocene–Pleistocene, J. Geophys. Res. 97 (1992) 11945–11982.
[26] L. Jolivet, C. Faccenna, Mediterranean extension and the Africa–Eurasia collision, Tectonics 19 (2000) 1095–1106.
[27] D.E. James, Andean crustal and upper mantle structure, J. Geophys. Res. 76 (1971) 3247–3271.
[28] S.L. Beck, G. Zandt, S.C. Myers, T.C. Wallace, P.G. Silver, L. Drake, Crustal-thickness variations in the central Andes, Geology 24 (1996) 407–410.
[29] E. Klosko, S. Stein, D. Hindle, J. Kley, E. Norabuena, T. Dixon, M. Liu, Comparison of GPS, seismological, and geological observations of Andean mountain building, in: S. Stein, J. Freymueller (Eds.), Plate Boundary Zones, Geodynamics Series vol. 30, A.G.U., Washington, 2002, pp. 123–134.
[30] R.M. Richardson, D. Coblentz, Constraint on the intraplate stress magnitudes from stress modeling in the Andes of South America, J. Geophys. Res. 99 (1994) 22015–22025.
[31] D. Coblentz, R.M. Richardson, Analysis of the South American intraplate stress field, J. Geophys. Res. 101 (1996) 8643–8657.
[32] G.A. Yañez, C.R. Ranero, R. von Huene, J. Diaz, Magnetic anomaly interpretation across the southern central Andes (32°–34°S): the role of the Juan Fernández Ridge in the late Tertiary evolution of the margin, J. Geophys. Res. 106 (2001) 6325–6345.

[33] P. Baby, P. Rochat, G. Mascle, G. Hérail, Neogene shortening contribution to crustal thickening in the back-arc of the Central Andes, Geology 25 (1997) 883–886.
[34] J. Kley, C.R. Monaldi, Tectonic shortening and crustal thickness in the Central Andes: how good is the correlation? Geology 26 (1998) 723–726.
[35] L.M. Cathles, The Viscosity of the Earth's Mantle, Princeton Univ. Press, Princeton, NJ, 1975.
[36] P. England, Comment on "Brittle failure in the upper mantle during extension of continental lithosphere" by Dale S. Sawyer, J. Geophys. Res. 91 (1986) 10487–10490.
[37] T. Sempere, G. Hérail, J. Oller, M.G. Bonhomme, Late Oligocene–Early Miocene major tectonic crisis and related basins in Bolivia, Geology 18 (1990) 946–949.
[38] T. Sempere, Phanerozoic evolution of Bolivia and adjacent regions, in: A.J. Tankard, R.J. Suarez, H.J. Welsink (Eds.), Petroleum Basins of South America, A.A.P.G. Memoir vol. 62, (1995) 207–230.
[39] S. Lamb, L. Hoke, L. Kennan, J. Dewey, Cenozoic evolution of the Central Andes in Bolivia and northern Chile, in: J.P. Burg, M. Ford (Eds.), Orogeny Through Time, Spec. Pub.-Geol. Soc., vol. 121, 1997, pp. 237–264.
[40] F. Pardo-Casas, P. Molnar, Relative motion of the Nazca (Farallon) and South American plates since Late Cretaceous time, Tectonics 6 (1987) 233–248.
[41] E. Norabuena, L. Leffler-Griffin, A. Mao, T. Dixon, S. Stein, I.S. Sacks, L. Occola, M. Ellis, Space geodetic observations of Nazca–South America convergence across the Central Andes, Science 279 (1998) 358–362.
[42] B. Isacks, Uplift of the central Andean plateau and bending of the Bolivian orocline, J. Geophys. Res. 93 (1988) 3211–3231.
[43] S. Wdowinski, Y. Bock, The evolution of deformation and topography of high elevated plateaus: 2. Application to the Central Andes, J. Geophys. Res., (1994) 7121–7130.
[44] L. Husson, T. Sempere, Thickening the Altiplano crust by gravity-driven crustal channel-flow, Geophys. Res. Lett. 30 (2003) 1243 (doi:10.1029/2002GL016877).
[45] C. Sue, P. Tricart, F. Thouvenot, J. Fréchet, Widespread extension in the core of the western Alps revealed by earthquake analysis, J. Geophys. Res. 104 (1999) 611–622.
[46] M. Sébrier, J.L. Mercier, F. Mégard, G. Laubacher, E. Carey-Gailhardis, Quaternary normal and reverse faulting and the state of stress in the Central Andes and South Peru, Tectonics 4 (1985) 739–780.
[47] M. Assumpçao, The regional intraplate stress field in South America, J. Geophys. Res. 97 (1992) 11889–11903.
[48] M.E. Beck, R.R. Burmester, R.E. Drake, P.D. Riley, A tale of two continents: some tectonic contrasts between the Central Andes and the North American Cordillera, as illustrated by their paleomagnetic signatures, Tectonics 13 (1994) 215–224.
[49] I. Coutand, A. Chauvin, P.R. Cobbold, P. Gautier, P. Ropperch, Vertical axis rotations across the Puna plateau (northwestern Argentina) from paleomagnetic analysis of Cretaceous and Cenozoic rocks, J. Geophys. Res. 104 (1999) 22965–22984.